Nanoscale

PAPER

View Article Online
View Journal | View Issue

Cite this: *Nanoscale*, 2023, **15**, 4448

Covalent post-assembly modification of π-conjugated supramolecular polymers delivers structurally robust light-harvesting nanoscale objects†

Victor Paulino,‡ Kaixuan Liu,‡ Valentino Cesiliano, Ifigeneia Tsironi, Arindam Mukhopadhyay, Maria Kaufman and Jean-Hubert Olivier *

A two-component stapling strategy is used to covalently tether a new class of water-soluble supramolecular polymers built from bay-functionalized perylene bisimide (PBI) units. By leveraging a novel combined strategy where excitonic coupling and fluorescence data are exploited as spectroscopic reporters, structural design principles are established to form light-harvesting superstructures whose ground-state electronic properties are not sensitive to solvation environments. Moreover, we interrogate the structural properties of stapled superstructures by capitalizing on the drastic changes in fluorescence quantum yields against parent supramolecular assemblies. In essence, our work shows that the combination of excitonic coupling measurements and photoluminescence experiments delineates a more accurate understanding of the design principles required to limit the degree of structural defects and magnify short- and long-range electronic couplings between redox-active units in this new class of solvated nanoscale objects. These results highlight that the fragile conformation of non-covalent assemblies, which are regulated by weak secondary interactions, can be preserved by post-assembly modification of preformed supramolecular polymers. These synthetic and spectroscopic principles can in turn be codified as experimental handles to parameterize the optoelectronic properties of light-harvesting nanoscale objects.

Received 5th December 2022,
Accepted 18th January 2023

DOI: 10.1039/d2nr06806k

rsc.li/nanoscale

Introduction

The tuneable photophysical and potentiometric properties of π-conjugated supramolecular polymers (π-SPs) built from stacks of redox-active chromophores make this class of materials appealing light-harvesting platforms for long-range energy transport and energy transduction purposes.[1–4] While long- and short-range electronic couplings between chromophores parameterize the photophysical properties of assemblies at nano- to microscale dimensions,[5,6] our ability to control these couplings by design is limited to a handful of strategies, which primarily rely on side-chain engineering, and control over aggregation pathways.[7–10] Despite these efforts, non-covalent interactions remain the main driving forces that regulate interchromophore couplings. Because non-covalent interactions are sensitive to experimental conditions,[11,12] subtle changes in temperature, solvent dielectric, and building-block concentrations alter the structure–function relationships of π-SPs.[13,14] These limitations often hamper the development of strategies to enforce strong interchromophore electronic couplings over a wide range of temperatures or solvent compositions.[15]

Covalent post-assembly modifications of π-SPs enable the formation of nanoscale objects equipped with emergent structure–function relationships. Conventional approaches have exploited one-component stapling methods that rely on photopolymerization and metal-catalysed cross-linking between reactive monomer units.[16,17] Although the formation of covalent bonds between building blocks has been shown to create hybrid assemblies equipped with functions not demonstrated by parent, non-covalent scaffolds, significant challenges remain. Specifically, for one-component stapling to operate successfully *via* photo-polymerization, reactive functional groups flanked on building blocks must adopt a precise conformation.[18–20] In contrast, the two-component stapling method showcased in Fig. 1A attaches freestanding tether units to non-covalent assemblies.[21–23] This method opens new avenues to modulate the (opto)electronic properties of π-SPs by

Department of Chemistry, University of Miami, Cox Science Centre, 1301 Memorial Drive, Coral Gables, FL 33146, USA. E-mail: jh.olivier@miami.edu

†Electronic supplementary information (ESI) available. See DOI: https://doi.org/10.1039/d2nr06806k

‡These authors contributed equally.

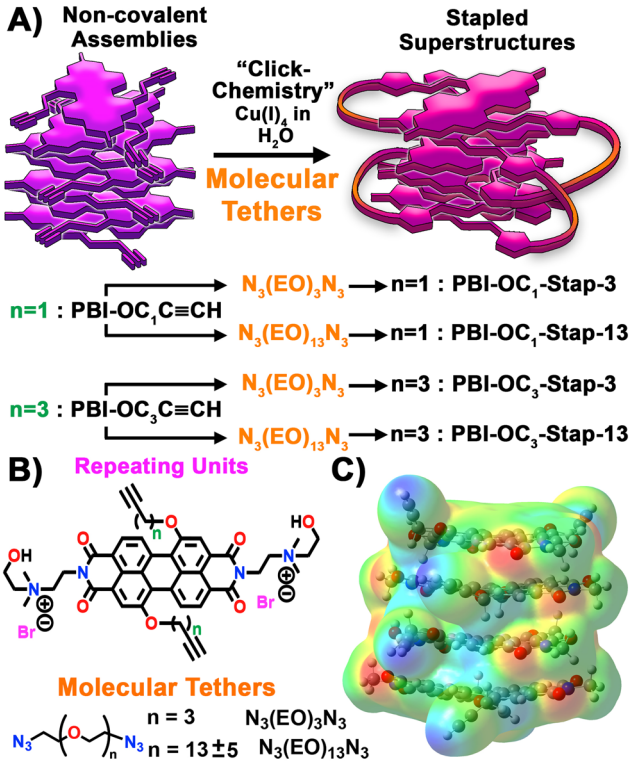

Fig. 1 (A) Schematized pathway to staple non-covalent assemblies initially formed in water with molecular tethers using copper(I)-catalysed "click-chemistry". Refer to the ESI† for synthetic details. Two non-covalent assemblies are used as precursors and are derived from the PBI units that feature ethynyl reactive side chains functionalized at the 1,7 positions (bay-functionalized) as shown in B. (C) Energy-minimized structure of a model tetramer aggregate featuring the **PBI-OC$_1$C≡CH** core. The corresponding electrostatic potential map is overlaid. Please see ESI† for more details.

exploiting the molecular tethers as synthetic handles. For example, we have shown that the structure of the tethers can be used to precisely control the ground- and excited-state electronic properties of stapled assemblies.[21] Others have recently capitalized on this methodology to engineer elegant solar energy transduction complexes.[24]

Herein, the scope of the two-component stapling method is expanded by elucidating how the monomer structures that comprise model π-SPs in conjunction with tether lengths regulate the photophysical properties of stapled assemblies. To do so, we use novel water-soluble π-SPs built from bay-functionalized perylene bisimide (PBI) units to highlight that the structure of the reactive side chains flanked on PBI building blocks is a structural component to regulate the interactions between π-conjugated cores in the final stapled assemblies. By using excitonic coupling as a spectroscopic marker, we establish structure–function relationships required to construct structurally rigid nanoscale objects whose ground-state electronic properties are not perturbed by the solvation environment. To reinforce these findings, we introduce steady-state fluorescence spectroscopy experiments on tethered assemblies as a tool to evaluate the level of structural defects, further informing on the efficiency of the stapling methodology. Compellingly, this combined approach allows the detection of defects at the termini of 1-dimensional stacks, which are dictated by the length of the molecular staplers and the PBI's reactive side chains. We posit that the combination of excitonic coupling measurements and photoluminescence properties offers more accurate insights into the structural attributes conferred by the tethers and the reactive side chains flanked on monomers.

Results and discussion

Synthesis and purification of stapled assemblies

The two PBI units **PBI-OC$_{1/3}$C≡CH** shown in Fig. 1B feature identical pendant ammonium side chains, but they differ from the length of the ethynyl-terminated alkoxy substituents attached to the PBI bay region. Due to the change of hydrophobic surfaces, these two building blocks assemble into supramolecular polymer precursors whose structures are different (*vide supra*). With these precursors in hand, we aim to elucidate the extent to which the structure–function relationships of non-covalent assembly precursors impact those of the tethered superstructures through the 2-component stapling method illustrated in Fig. 1A. An energy-minimized non-covalent tetramer model derived from the **PBI-OC$_1$C≡CH** building blocks is shown in Fig. 1C and highlights the conformation adopted by the reactive ethynyl functions around the rigid π-conjugated cores. As established by us and others,[25–27] electrostatic interactions between the repeating units govern the structure of π-conjugated supramolecular polymers. See section 9 of the ESI† for more details. While probing the aggregation mechanism of the two bay-functionalized PBI monomers using temperature-dependent studies revealed unsuccessful (Fig. S4†), denaturation studies using DMF as a "good solvent" and H_2O as a "bad solvent" confirms the existence of non-covalent assemblies in aqueous media. As shown in Fig. 2A, the addition of DMF solvent into a solution of the **PBI-OC$_3$C≡CH** aggregate in H_2O is accompanied by the concomitant rise and decrease of the 0–0 and 0–1 vibronic transitions centered at 571 nm and 534 nm, respectively. Notably, the **PBI-OC$_3$C≡CH** unit exhibits the spectroscopic hallmarks of a molecularly dissolved species in DMF as confirmed by: (1) the ratio of 0–0 and 0–1 vibronic transition is 1.4, and (2) the energetic spacing between the 0–0, 0–1, and 0–2 vibronic transitions is constant (ΔE = 170 meV) and corresponds to aromatic C=C stretching modes.[28,29] Similar observations are made for the **PBI-OC$_1$C≡CH** analog and are detailed in section 4 of the ESI.†

The degree of aggregation (α) as a function of solvent composition is shown in Fig. 2B for the **PBI-OC$_3$C≡CH** unit and is used to gain insights into the assembly pathway. The equilibrium model introduced by Korevaar and Meijer reveals that an isodesmic growth mechanism (σ = 1) is at the origin of the formation of this π-SP.[30] Similar analyses are shown for the

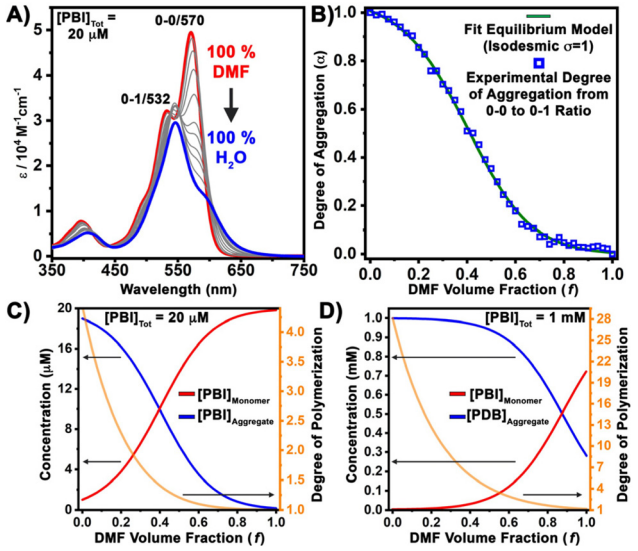

Fig. 2 (A) Solvent-dependent UV-vis spectra that chronicle the aggregation of a 20 μM solution of **PBI-OC$_3$C≡CH** as a function of the ratio of H_2O (bad solvent) in DMF (good solvent). (B) Experimental degree of aggregation (open blue square) as a function of DMF volume ratio (f) in water. An isodesmic equilibrium model (σ = 1) best fit the experimental data. (C and D) concentration of the free monomer ([PBI]monomer) and the monomers that exist in an aggregated state ([PBI]aggregate) as a function of DMF volume fraction with $[PBI]_{Tot}$ = 20 μM (C) and $[PBI]_{Tot}$ = 1 mM. Note the concentration of PBI has been calculated using UV-vis data.

Table 1 Thermodynamic parameters estimated from the fitting of the solvent-dependent UV-vis data. DP = degree of polymerization

Fitting parameters	PBI-OC$_1$C≡CH	PBI-OC$_3$C≡CH
σ	1	1
$\Delta G°$ (kJ mol^{-1})	−29.05	−33.00
m (kJ mol^{-1})	18.59	19.91
K_e (mol^{-1})	1.5×10^5	7.64×10^5
DP at 1 mM	13	28

PBI-OC$_1$C≡CH building block in section 4 of the ESI.† Table 1 summarizes the thermodynamic parameters calculated using the equilibrium model for the two supramolecular polymer precursors. Specifically, the calculated elongation constant (K_e) highlights the difference in the PBI core's structure. Indeed, the **PBI-OC$_3$C≡CH** unit is characterized by a K_e (7.64×10^5 M^{-1}) higher than that evidenced by the **PBI-OC$_1$C≡CH** unit ($K_e = 1.51 \times 10^5$ M^{-1}). Lengthening the carbon chains attached to the PBI bay region increases the hydrophobic interactions between repeating units. Please note that these calculated elongation constants fall in line with those published by us and others on the assembly of amphiphilic PBI units in water.[25,31–33] Congruently, the π-SPs built from the **PBI-OC$_3$C≡CH** units at 1 mM in H_2O comprise a larger number of repeating units (DP = 28) than that featured in the **PBI-OC$_1$C≡CH** analog (DP = 13), as shown in Fig. 2C and D. Accordingly, parent assemblies **[PBI-OC$_3$C≡CH]$_{28}$** and **[PBI-OC$_1$C≡CH]$_{13}$** π-SPs are employed as molecular templates to construct the stapled superstructures *via* the post-assembly modification procedure shown in Fig. 1A, where the molecular tethers **N$_3$(EO)$_{13}$N$_3$** and **N$_3$(EO)$_3$N$_3$** are reacted with the supramolecular precursors initially formed in water using Cu^{I}-catalyzed "click" chemistry conditions. For detailed procedures, refer to section 2 of the ESI.† After a 16-hour reaction time, the stapled assemblies are pre-purified using membrane filtration to remove unreacted building blocks, and nanoscale objects smaller than the molecular weight cut-off of the membrane (10 000 Da). Gel permeation chromatography using Sephacryl S-200 as a stationary phase allows isolation of stapled assemblies. In a nutshell, this process allows us to remove unreacted building blocks, catalyst-derived species, and larger objects that may form during the tethering step.[34,35]

Analyses of the four stapled superstructures using gel permeation chromatography reveal important structural parameters, which are mainly governed by molecular tethers. The two tethered assemblies **PBI-OC$_{1/3}$-Stap-13** exhibit weight-average molecular weights ($\bar{M}_w$) larger than those estimated for the two **PBI-OC$_{1/3}$-Stap-3** assemblies. See Table S1 in section 5 of the ESI.† Derived from identical PBI cores, the **PBI-OC$_1$-Stap-13** construct comprises, on average, more repeating units (n = 12) when compared to those estimated in the **PBI-OC$_1$-Stap-3** analog (n = 10). A similar observation is made when assessing the number of repeating units that built the stapled **PBI-OC$_3$-Stap-13** (n = 12) and **PBI-OC$_3$-Stap-3** (n = 10) constructs. From these findings, we conclude that the degree of supramolecular polymerization (DP in Table 1) of the non-covalent precursors does not significantly alter the number of repeating units in the respective final, stapled superstructures but rather it is the length of the molecular linker that controls the size of the stapled superstructures in solution.

Solid-state morphological characterization

The solid-state morphologies of the stapled assemblies probed by atomic force microscopy (AFM) confirm the formation of discrete nanoscale objects whose thicknesses have been estimated by performing statistical analyses.[36,37] The **PBI-OC$_3$-Stap-3** assemblies form the microscale 1-dimensional objects shown in Fig. 3A and S16.† Using these structures, a statistical thickness of 2.4 nm is calculated, which we assign to the diameter of one stapled assembly. The energy-minimized DFT model shown in Fig. S31† validates this claim. We posit that the **PBI-OC$_3$-Stap-3**-derived microstructures shown in Fig. 3A originate from lateral interactions between the stapled assemblies during the drop-casting process. The tethered **PBI-OC$_3$-Stap-13** analogs built with the longer, more flexible linkers (EO)$_{13}$ initiate the formation of the wire-like structures observed in Fig. 3B and S17.† It is interesting to note that the statistical thickness of these nanostructures is 4.0 nm, larger than that calculated for the **PBI-OC$_3$-Stap-3**.

The apparent thickening of the **PBI-OC$_3$-Stap-13** constructs originates from the structural properties of the tethers. Congruent with the expectation that the longer, more flexible (EO)$_{13}$ linker occupies a larger volume around the PBI cores, it

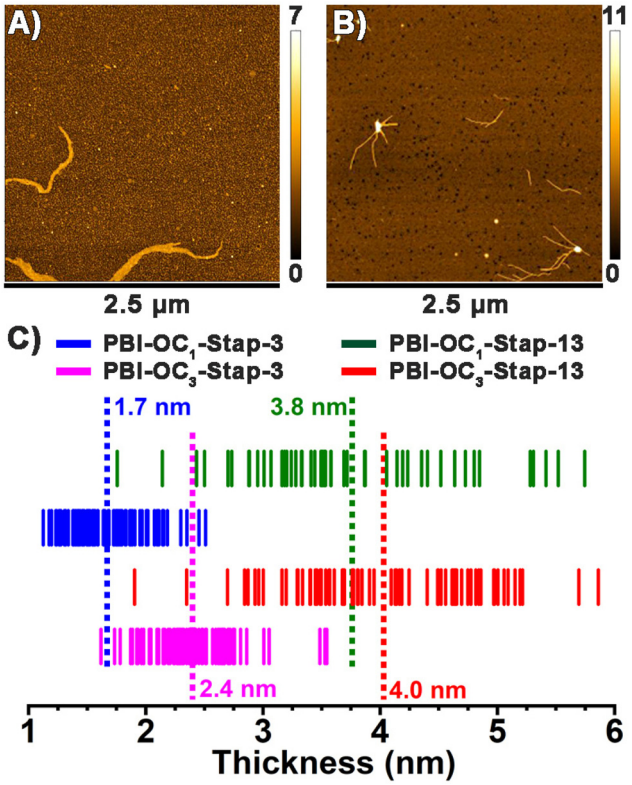

Fig. 3 (A, B) Atomic force microscopy images recorded for the **PBI-OC$_3$-Stap-3** (A) and **PBI-OC$_3$-Stap-13** (B) assemblies drop casted on silicon substrates from a water solution. (C) Distribution of the nanostructure thicknesses recorded for the **PBI-OC$_1$-Stap-3/13** and **PBI-OC$_3$-Stap-3/13** assemblies. The dotted lines represent the average calculated from each measured population.

is expected for the **PBI-OC$_3$-Stap-13** constructs to be thicker than the stapled **PBI-OC$_3$-Stap-3** assemblies. A similar trend is observed for the tethered assemblies derived from the **PBI-OC$_1$** core, although we note that their solid-state morphologies differ from that observed for the **PBI-OC$_3$**-derived cores. As captured in Fig. S14,† the **PBI-OC$_1$-Stap-3** assemblies form worm-like structures with a statistical thickness of 1.7 nm. It is interesting to note that the **PBI-OC$_1$-Stap-13** assemblies form the discrete structures shown in Fig. 3B and S15.† These constructs are thicker than the **PBI-OC$_1$-Stap-3** assemblies (3.8 nm, Fig. 3C), an observation that highlights the structural properties conferred by the tethers. Furthermore, the PBI-OC$_1$ core produces stapled assemblies that are, on average, thinner than those formed by the PBI-OC$_3$ core. This observation highlights the contributions arising from divergent hydrophobicity of the reactive side chains in the overall stapled assembly structures.

All taken together, the structural insights gleaned by AFM allow us to validate the tethering of individualized supramolecular polymers. If cross-linking reactions between the tethers and the solubilized stacks were the major reaction pathways (inter-stack reticulation), we would expect to witness larger structures associated with a broader distribution of measured thicknesses. The fact that the tethered **PBI-OC$_1$-Stap-3** and **PBI-OC$_3$-Stap-3** assemblies exhibit an average thickness similar to the width of one PBI building block modeled using DFT (see section S9†) further validates the efficiency of the stapling toward intra-stack reactivity. Furthermore, the consistent thickening of the **PBI-OC$_{1/3}$-Stap-13** assemblies as compared to the **PBI-OC$_{1/3}$-Stap-3** analogs is rationalized by the structure of the longer, more flexible (EO)$_{13}$ molecular tethers. This linker occupies a larger volume around the rigid π-conjugated core than the short, more rigid (EO)$_3$ linker, and it can sample wider conformation populations. While we cannot rule out the formation of larger structures stemming from the tethering between stacks, we posit that if these larger objects were formed, they would be separated from the initial samples during the GPC purification steps. Consequently, they do not plague the structural and photophysical analyses performed in this study.

Using scanning electron microscopy (SEM), the solid-state morphologies of the supramolecular precursors are compared to those of the tethered assemblies to decipher any structural properties conferred by the ethylene oxide linkers at micro-scale dimensions. As seen in Fig. 4A and D, the two supramolecular precursors dropcast from parent water solutions form elongated objects whose lengths are ranging from 1 μm to 10 μm. We note that the structure of the side chain on the PBI monomers does not play a significant role in dictating the solid-state morphologies of the non-covalent assembly. The stapled **PBI-OC$_3$-Stap-3** and **PBI-OC$_3$-Stap-13** platforms lack the ability to form well-defined hierarchical domains in the solid state and evolve into the aggregated structures shown in Fig. 4E and F and in section 6 of the ESI.† The raft-like features observed in Fig. 4E may originate from the interaction of the wire-like structures observed by AFM, while the aggregated structures highlighted in Fig. 4F are most likely to represent the evolution of the nanostructures evidenced in Fig. 4A. The solid-state samples are made by drop casting techniques where heterogeneous concentration profiles exist during solvent evaporation, which can engender different interaction modes between the stapled assemblies.

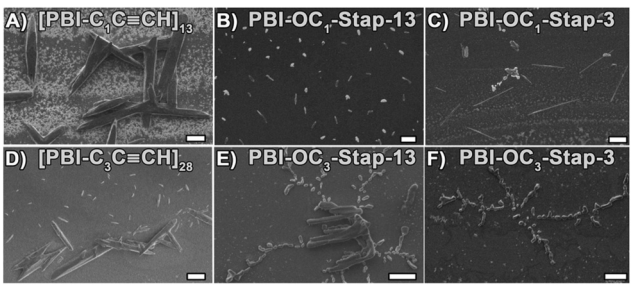

Fig. 4 SEM images highlighting the solid-state morphologies recorded for drop cast aqueous solutions of the parent non-covalent precursors (A) **PBI-OC$_1$C≡CH**, (D) **PBI-OC$_3$C≡CH**. Representative SEM images recorded for assemblies stapled with the long tether **N$_3$(EO)$_{13}$N$_3$** (B) **PBI-OC$_1$-Stap-13**, and (E) **PBI-OC$_3$-Stap-13**, and the short tether **N$_3$(EO)$_3$N$_3$** (C) **PBI-OC$_1$-Stap-3**, and (F) **PBI-OC$_3$-Stap-3**. Scale bars are 2 μm. Additional SEM images are shown in Section 6 of the ESI.†

Wire-like superstructures are visible for the drop cast **PBI-OC$_1$-Stap-3** and **PBI-OC$_1$-Stap-13** samples in Fig. 4B and C. It is interesting to note that longer microwires (>10 mm) are observed for the **PBI-OC$_1$-Stap-3** construct. It is fair to assume that the short molecular tether combined with the short side chain anchored at the PBI's bay positions enables the stapled **PBI-OC$_1$-Stap-3** assemblies to adopt more rigid, constrained conformations, which engender the hierarchical microstructures observed by SEM in the solid state. Furthermore, we suggest that the worm-like domains observed by AFM in the **PBI-OC$_1$-Stap-3** samples are built from individual stapled constructs, which exhibit varying degrees of lateral interactions through the ethylene oxide linkers. The microstructures observed by SEM provide a better representation of the bulk solid state morphologies while the nanostructures unraveled by AFM may overlook the roles played by lateral interactions between the stapled assemblies. From these SEM and AFM investigations, we postulate that a synergistic effect between the side chain structures and the length of the molecular tethers is at the origin of the difference in the solid-state morphologies observed for the stapled constructs.

Ground-state electronic characterization

Ground-state electronic absorption spectroscopy (EAS) is used to interrogate the structural robustness of the stapled assemblies against solvent composition. As gleaned in Fig. 5, the tethered assemblies evidence the spectroscopic signatures of aggregated species in a solvent (DMF) that promote dissociation of the control, non-covalent assemblies. Notably, the spectra recorded for the parent **PBI-OC$_{1/3}$C≡CH** assemblies solvated in 90% DMF in water (Fig. 5) show the hallmark of individualized species (*vide infra*) while the absorptive features observed for the four stapled superstructures in Fig. 5 indicate the existence of electronically coupled PBI units. Indeed, the ratio of the 0–0 and 0–1 vibronic transition is well below one and highlights the redistribution of the 0–0 oscillator strength into the 0–1 transition, a hallmark of positive excitonic coupling in H-like aggregates.[8,38,39] Moreover, the broadening of the line shapes associated with the electronic transition from the ground- to the first-excited state manifold diagnoses a change of rotational offsets between interacting PBI cores, an experimental observable further confirming the existence of H-like aggregates in DMF.[31] To summarize, in a good solvent that promotes dismantlement of the non-covalent precursors, the stapled superstructures **PBI-OC$_{3/1}$-Stap-13/3** preserve their aggregated states due to the existence of covalent tethers that maintain structural integrity.

To quantify the extent to which the molecular tethers and the structure of the PBI building blocks parameterize the interactions between chromophores as a function of solvent composition, we have estimated the excitonic coupling (J_{12}) between PBI units in the stapled assemblies and the control analogs (Table 1) in water and in DMF.[25,33,40] In water, the two non-covalent controls are aggregated and feature similar J_{12} values that are weaker than those measured for the stapled assemblies; this finding indicates that the covalent tethers force stronger inter-chromophore interactions. Noteworthy, the linker **N$_3$(EO)$_3$N$_3$**, having a lower degree of conformational freedom, promotes the strongest coupling in the **PBI-OC$_1$-Stap-13/3** and **PBI-OC$_3$-Stap-13/3** series, 125 and 117 meV, respectively. Compellingly, the side chains flanked at the 1,7 position on the PBI units act on the magnitude of J_{12}. In water, the stapled assemblies **PBI-OC$_1$-Stap-13/3** built from the shorter side chains demonstrate a stronger J_{12} than that estimated for the tethered constructs **PBI-OC$_3$-Stap-13/3** derived from the propoxy (–OC$_3$) side chain. These measurements underscore that a short molecular tether combined with a short side chain flanked on the bay functionalized PBI is a valid structural design principle to increase inter-chromophore interactions in stapled assemblies solvated in an aqueous medium.

The structural robustness conferred by the covalent tethers in the **PBI-OC$_3$-Stap-13/3** and **PBI-OC$_1$-Stap-13/3** assemblies is further confirmed by investigating J_{12} in DMF solvent. As seen in Table 2, the stapled assemblies evidence a positive J_{12} in a solvation environment (90% DMF in H$_2$O) where the non-covalent control assemblies dissociate into monomeric units. The fact that the J_{12} values calculated for the **PBI-OC$_1$** series in

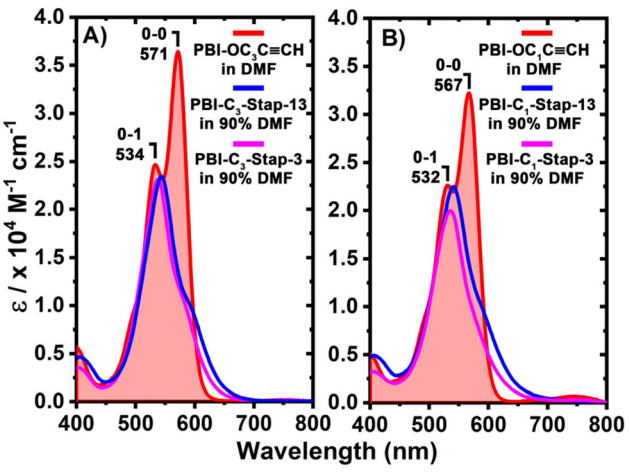

Fig. 5 (A, B) Ground-state electronic absorption spectra of the precursor building block **PBI-OC$_{3/1}$C≡CH** (red trace), and the corresponding stapled assemblies **PBI-OC$_{3/1}$-Stap-13** (blue trace), and **PBI-OC$_{3/1}$-Stap-3** (purple trace) in 90% DMF in H$_2$O solvent mixture.

Table 2 Excitonic coupling (J_{12}) in meV as a function of molecular tethers and solvent calculated for the stapled assemblies and the non-covalent analogues using the oscillator strength ratio of the 0–0 and 0–1 vibronic transitions calculated by deconvolution of electronic ground state absorption spectra. Please refer to section 7 of the ESI†

		DMF	H$_2$O
PBI-OC$_1$-	Non-Cov	n/a	96
	Stap-3	114	125
	Stap-13	95	118
PBI-OC$_3$-	Non-Cov	n/a	89
	Stap-3	111	117
	Stap-13	107	107

DMF are modestly weaker than those in H_2O points to conformational changes of the stapled **PBI-OC$_1$-Stap-13/3** constructs as a function of the solvation environment. The ethylene oxide linkers can adopt different conformations in DMF due to the absence of hydrogen bonds provided by the aqueous medium.[41,42] This structural perturbation can exert forces on the rigid PBI cores, which consequently alters inter-chromophore interactions. In contrast, the **PBI-OC$_3$-Stap-13/3** assemblies are less prone to conformational changes, as these superstructures evidence a J_{12} in DMF comparable to that assessed in H_2O (Table 2). These data indicate that the longer propoxy side chains connecting the ethylene oxide linkers to the rigid PBI cores can buffer structural perturbations induced by a change of solvation environments.

Photoluminescence experiments reveal structural robustness

Steady-state fluorescence spectroscopy experiments were performed to gain insights into the excited-state electronic properties of the tethered assemblies. The emission spectra recorded for the parent non-covalent assemblies in water are shown in Fig. 6A and S28A† and resemble those acquired for the monomeric units solvated in DMF (Fig. 6B and S28B†). To complement this observable, a drastic decrease in the fluorescence quantum yield (Φ^F) is noted for the parent supramolecular polymers **PBI-OC$_1$C≡CH** (Φ_{H_2O} = 4.5%) and **PBI-OC$_3$C≡CH**($\Phi^F_{H_2O} = 5\%$) when compared to those recorded for the monomeric species solvated in DMF solvent. See Table 3. We posit that the emission spectrum recorded for the parent supramolecular polymers in H_2O originates from residual monomeric building blocks, which are not part of non-covalent aggregates. This claim relies on the fact that dynamic equilibrium regulates the formation of non-covalent assemblies.[43,44] Please note that the steady-state emission spectra have been recorded using a 1 μM concentration solution of the building block to avoid reabsorption phenomenon. Considering that both supramolecular polymers are characterized by a $k_e \sim 10^5\ M^{-1}$, it is unlikely that at 1 μM concentration all the building blocks are under an aggregated state. Furthermore, the excitation spectra recorded for the parent supramolecular polymers (Fig. 6A and S28A†) are reminiscent of the absorption spectra of individualized monomers.[45,46] For the non-covalent aggregated structures, we note the absence of broad and featureless emission signatures that expand in the NIR spectral window, which are features diagnostic of excimer state formation. While excimers are well-known to characterize the excited-state properties of PBI-derived aggregates, alternative excited-state deactivation channels exist in the bay-functionalized PBI assemblies. Based on previous studies, excited states with significant charge-transfer characters could rationalize the lack of excimer state formation.[47–50]

Table 3 Fluorescence quantum yields (Φ^F) of the parent non-covalent assemblies and the stapled constructs measured in water and DMF solvent (90% DMF/10% H_2O) after photoexcitation at 545 nm

		DMF	H_2O
PBI-OC$_1$-	Non-Cov	45.0% ± 3.2	4.5% ± 0.18
	Stap-3	1.2% ± 0.23	0.5% ± 0.02
	Stap-13	8.7% ± 0.3	1.2% ± 0.03
PBI-OC$_3$-	Non-Cov	43% ± 2.9	5.1% ± 0.2
	Stap-3	2.2% ± 0.2	0.8% ± 0.03
	Stap-13	7.9% ± 0.9	1.5% ± 0.06

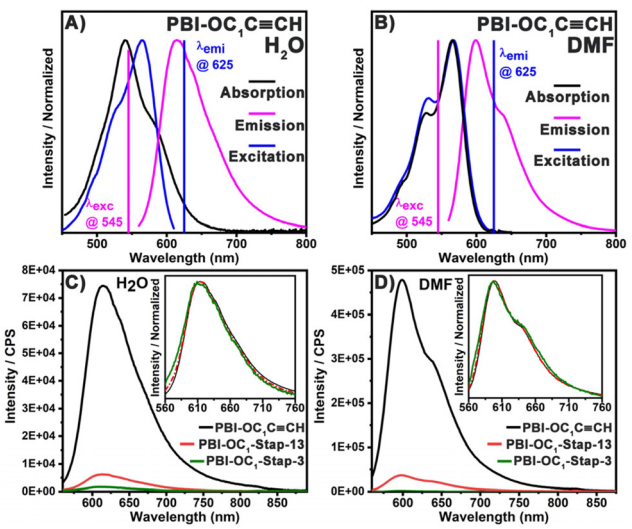

Fig. 6 Normalized emission (λ_{exc} = 545 nm) and excitation spectra (λ_{emi} = 625 nm) of the precursor building block **PBI-OC$_1$C≡CH** solvated in water (A) and DMF solvent (90% DMF/10% H_2O) (B). The normalized absorption spectra are shown as visual aids in the insets. (C and D) Steady-state photoluminescence spectra (λ_{exc} = 545 nm) of the stapled assemblies **PBI-OC$_1$-Stap-1/13** are compared to that of the parent non-covalent precursors **PBI-OC$_1$C≡CH** in water (C) and DMF solvent (90% DMF/10% H_2O) (D). The concentration of the three samples is kept identical at 1 μM of PBI building blocks.

As shown in Fig. 6C, the photoluminescence spectra for the **PBI-OC$_1$-Stap-3/13** constructs solvated in water are identical to those of the parent non-covalent assemblies in Fig. 6A. However, a drastic decrease in the emission intensity is noted. An identical observation is made for the **PBI-OC$_3$-Stap-3/13** analogs as shown in Fig. S29.† Congruently, the stapled assemblies **PBI-OC$_{1/3}$-Stap-3/13** exhibit lower fluorescent quantum yields in water (Table 3) as compared to their respective parent, non-covalent assemblies. Because samples made of the solvated tethered superstructures are purified using membrane centrifugation and gel permeation chromatography, they are not contaminated with monomeric, untethered building blocks removed during the purification process. Consequently, we stress that the reported spectroscopic data report exclusively on the properties of the stapled assemblies. The residual monomer-like emission recorded for the stapled assemblies is assigned to end defects in the tethered structures.[51,52] It is unlikely that all the PBI monomer featured in stapled assemblies are covalently attached through the reaction of the two ethynyl reactive side chains as schematized in Fig. 7. In other words, the PBI building blocks at the termini of tethered stacks may be covalently attached through only one triazole connectivity

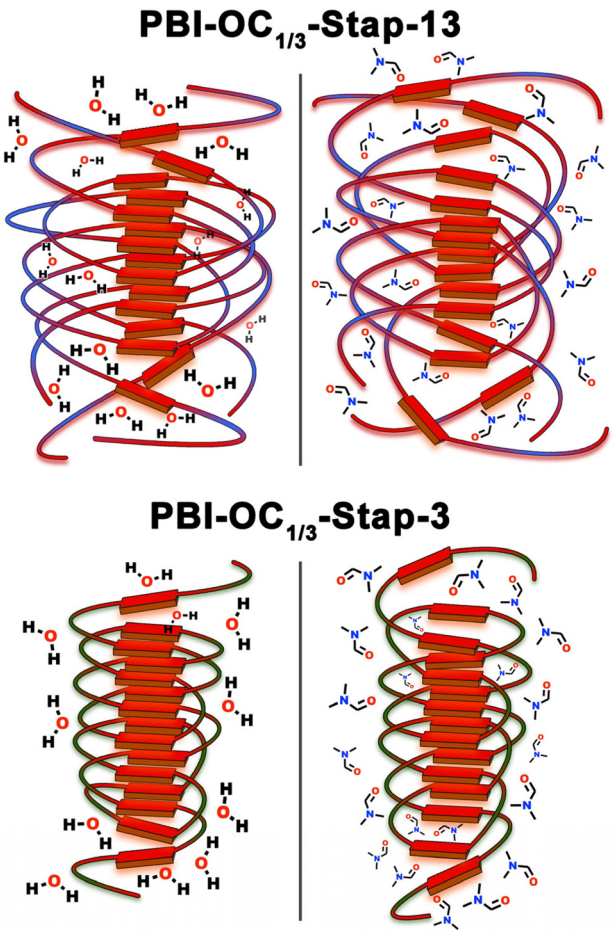

Fig. 7 Schematic illustration of the tethered assemblies and their end defects as a function of the solvation environment. Namely, partially bound PBI units at the termini of stapled stacks are suggested to have various degree of monomer-like character in DMF and water solvent.

as opposed to two triazole groups for PBI building blocks featured towards the center of the stapled superstructures. Consequently, the loosely bound PBI units at the termini of tethered stacks may sample different degrees of solvation to those in the center of the stacks as represented in Fig. 7.

When compared to the parent, non-covalent precursors, the lower Φ^F calculated for the **PBI-OC$_{1/3}$-Stap-3/13** stapled assemblies originates from the lack of monomeric species contributing to the overall emission intensity. In essence, our stapling methodology allows the formation of more homogeneous samples. The fact that the tethered superstructures built from the longer molecular linker $(EO)_{13}$ manifest a Φ^F modestly larger than that reported for the **PBI-OC$_{1/3}$-Stap-3** trace its origin from the structural properties of the covalent linker. The shorter $(EO)_3$ tether reduces structural defects at the end of the stapled assemblies, as shown in Fig. 7, limiting the degree of solvation of the loosely bound PBI at the end of a stack. In contrast, the longer, more flexible tether $(EO)_{13}$ imposes a lower degree of structural rigidity, consequently engendering structures where more pronounced structural perturbations are possible.

In DMF, the emission spectra of the parent precursor **PBI-OC$_{1/3}$C≡CH** and the associated Φ^F are reminiscent of solvated, individualized PBI units. Interestingly, the emission spectra recorded for the stapled assemblies **PBI-OC$_1$-Stap-3/13** in DMF (Fig. 6D) mimic those of the parent precursors, but a drastic decrease in the Φ^F of the tethered superstructures is witnessed (Table 3). An identical trend is observed for the **PBI-OC$_3$-Stap-3/13** analogs as shown in Fig. S29.† Interestingly, the **PBI-OC$_{1/3}$-Stap-3** species exhibit lower Φ^F_{DMF} of 1.16% and 2.15%, respectively, when compared to the **PBI-OC$_{1/3}$-Stap-13** superstructures tethered with the long, more flexible linker, Φ^F_{DMF} = 8.65% and 7.86%, respectively. As rationalized for the water-solvated assemblies, the monomer-like emission observed for the **PBI-OC$_{1/3}$-Stap-3/13** constructs likely originates from end defects. However, larger structural perturbations occur in DMF than those happening in a bad solvent (water). As demonstrated earlier, DMF is a "good" solvent, which promotes the dissociation of non-covalent assemblies. In this medium, the covalent linkers are the sole factors that prevent the dismantlement of the π-conjugated stacks into molecularly dissolved species. All taken together this data indicates that the DMF solvent accentuates the structural perturbation between the assemblies tethered with the long and short linkers as schematized in Fig. 7. Furthermore, the photoluminescence properties of the stapled assemblies point to the same conclusion as that made from the excitonic coupling measurements. Namely, the shorter tether $(EO)_3$ enables the formation of more structurally robust assemblies than the more flexible tethers $(EO)_{13}$ allow. We suggest that the shorter tether not only increases interactions between building blocks as previously shown by us but also reduces structural defects at the end of the stapled stacks.

Conclusions

In conclusion, we used a new class of supramolecular polymers as templates to form stapled superstructures. The structure and electronic properties of these nanoscale objects can be precisely tuned by the length of the molecular tethers and the functionality of redox-active building blocks. Notably, the number of repeating units in the tethered assemblies is primarily parameterized by the structure of the molecular tethers and not by the number of repeating units comprised in the supramolecular polymer precursors, as initially hypothesized. We show that the structural robustness conferred by the covalent tethers preserves the strong electronic coupling in the stapled assemblies in solvation environments where supramolecular polymers dissociate into individualized repeating units. Specifically, excitonic coupling measurements demonstrate that not only the length of the molecular tethers is an important structural parameter that enables tuning the electronic interaction between building blocks, but also that the length of the alkoxy side chains on the PBI building blocks is a structural handle to be considered when engineering functional tethered assemblies.

Furthermore, we highlight that steady-state fluorescence spectroscopy experiments performed with the stapled assemblies enable the interrogation of structural end defects, which ground-state electronic absorption spectroscopy cannot inform on. The drastic decrease in the emission quantum yields measured for the tethered constructs in DMF and water solvents indicates that the 2-component stapling methodology allows the formation of homogeneous samples, which are not contaminated by monomeric building blocks. Consequently, the monomer-like emissions reported for the stapled assemblies inform on (1) structural reorganization enforced by solvation environments, and (2) the existence of loosely bound building blocks at the termini of the tethered stacks. Compellingly, the assemblies build with a combination of a rigid linker and a shorter side chain exhibit emission quantum yields weaker than that measured for constructs built with a more flexible stapler and a longer side chain. This observation corroborates conclusions made from excitonic coupling measurements and further highlights cardinal design principles to engineer rigid light-harvesting nanoscale objects in solution.

Author contributions

All the authors contributed to the scientific ideas and research. V. P. and J. H. O. wrote and reviewed the manuscript.

Conflicts of interest

There are no conflicts to declare.

Acknowledgements

This work is supported by the National Science Foundation through the NSF CAREER award 1941410.

References

1 J. R. Caram, S. Doria, D. M. Eisele, F. S. Freyria, T. S. Sinclair, P. Rebentrost, S. Lloyd and M. G. Bawendi, *Nano Lett.*, 2016, **16**, 6808–6815.
2 A. P. Deshmukh, N. Geue, N. C. Bradbury, T. L. Atallah, C. Chuang, M. Pengshung, J. Cao, E. M. Sletten, D. Neuhauser and J. R. Caram, *Chem. Phys. Rev.*, 2022, **3**, 021401.
3 Y. Wan, A. Stradomska, J. Knoester and L. Huang, *J. Am. Chem. Soc.*, 2017, **139**, 7287–7293.
4 O. P. Dimitriev, J. Zirzlmeier, A. Menon, Y. Slominskii and D. M. Guldi, *J. Phys. Chem. C*, 2021, **125**, 9855–9865.
5 N. J. Hestand and F. C. Spano, *Chem. Rev.*, 2018, **118**, 7069–7163.
6 M. Balooch Qarai, X. Chang and F. C. Spano, *J. Chem. Phys.*, 2020, **153**, 244901.
7 M. R. Wasielewski, *Acc. Chem. Res.*, 2009, **42**, 1910–1921.
8 D. Bialas, E. Kirchner, M. I. S. Röhr and F. Würthner, *J. Am. Chem. Soc.*, 2021, **143**, 4500–4518.
9 J. M. Lim, P. Kim, M.-C. Yoon, J. Sung, V. Dehm, Z. Chen, F. Würthner and D. Kim, *Chem. Sci.*, 2013, **4**, 388–397.
10 K. Balakrishnan, A. Datar, T. Naddo, J. Huang, R. Oitker, M. Yen, J. Zhao and L. Zang, *J. Am. Chem. Soc.*, 2006, **128**, 7390–7398.
11 K. Liu, A. Levy, C. Liu and J.-H. Olivier, *Chem. Mater.*, 2018, **30**, 2143–2150.
12 C. Liu, K. Liu, A. Mukhopadhyay, V. Paulino, B. Bernard and J.-H. Olivier, *Organometallics*, 2020, **39**, 2984–2990.
13 T. F. A. De Greef, M. M. J. Smulders, M. Wolffs, A. P. H. J. Schenning, R. P. Sijbesma and E. W. Meijer, *Chem. Rev.*, 2009, **109**, 5687–5754.
14 G. Ghosh, P. Dey and S. Ghosh, *Chem. Commun.*, 2020, **56**, 6757–6769.
15 C. Kulkarni, K. K. Bejagam, S. P. Senanayak, K. S. Narayan, S. Balasubramanian and S. J. George, *J. Am. Chem. Soc.*, 2015, **137**, 3924–3932.
16 T. Yamamoto, T. Fukushima, Y. Yamamoto, A. Kosaka, W. Jin, N. Ishii and T. Aida, *J. Am. Chem. Soc.*, 2006, **128**, 14337–14340.
17 J. Seo, J. F. Joung, S. Park, Y. J. Son, J. Noh and J.-M. Kim, *Nat. Commun.*, 2020, **11**, 6260.
18 Z. Li, F. W. Fowler and J. W. Lauher, *J. Am. Chem. Soc.*, 2009, **131**, 634–643.
19 E. Jahnke, I. Lieberwirth, N. Severin, J. P. Rabe and H. Frauenrath, *Angew. Chem., Int. Ed.*, 2006, **45**, 5383–5386.
20 J. Fan, X. Xu, W. Yu, Z. Wei and D. Zhang, *Polym. Chem.*, 2020, **11**, 1947–1953.
21 A. Ashcraft, K. Liu, A. Mukhopadhyay, V. Paulino, C. Liu, B. Bernard, D. Husainy, T. Phan and J.-H. Olivier, *Angew. Chem., Int. Ed.*, 2020, **59**, 7487–7493.
22 V. Paulino, D. M. Cadena, K. Liu, A. Mukhopadhyay, S. T. Roberts and J.-H. Olivier, *Chem. Mater.*, 2022, **34**, 6518–6528.
23 M. Tan, M. Takeuchi and A. Takai, *Chem. Sci.*, 2022, **13**, 4413–4423.
24 T. Gobbato, F. Rigodanza, E. Benazzi, P. Costa, M. Garrido, A. Sartorel, M. Prato and M. Bonchio, *J. Am. Chem. Soc.*, 2022, **144**, 14021–14025.
25 K. Liu, V. Paulino, A. Mukhopadhyay, B. Bernard, A. Kumbhar, C. Liu and J.-H. Olivier, *Phys. Chem. Chem. Phys.*, 2021, **23**, 2703–2714.
26 C. R. Martinez and B. L. Iverson, *Chem. Sci.*, 2012, **3**, 2191–2201.
27 V. Paulino, A. Mukhopadhyay, I. Tsironi, K. Liu, D. Husainy, C. Liu, K. Meier and J.-H. Olivier, *J. Phys. Chem. C*, 2021, **125**, 10526–10538.
28 W. Wang, J. J. Han, L.-Q. Wang, L.-S. Li, W. J. Shaw and A. D. Q. Li, *Nano Lett.*, 2003, **3**, 455–458.
29 J. Chen, A. W. Ziegler, B. Zhao, W. Wan and A. D. Q. Li, *Chem. Commun.*, 2017, **53**, 4993–4996.
30 P. A. Korevaar, C. Schaefer, T. F. A. de Greef and E. W. Meijer, *J. Am. Chem. Soc.*, 2012, **134**, 13482–13491.

31 G. L. Eakins, J. K. Gallaher, R. A. Keyzers, A. Falber, J. E. A. Webb, A. Laos, Y. Tidhar, H. Weissman, B. Rybtchinski, P. Thordarson and J. M. Hodgkiss, *J. Phys. Chem. B*, 2014, **118**, 8642–8651.
32 E. Krieg, H. Weissman, E. Shimoni, A. Bar On and B. Rybtchinski, *J. Am. Chem. Soc.*, 2014, **136**, 9443–9452.
33 K. Liu, A. Mukhopadhyay, A. Ashcraft, C. Liu, A. Levy, P. Blackwelder and J.-H. Olivier, *Chem. Commun.*, 2019, **55**, 5603–5606.
34 X. Qin, K. Wang, X. Chen, Y. Qu, L. Li and T. Kuang, *Photosynth. Res.*, 2006, **90**, 195–204.
35 N. Zhang, C. Zhang, Y. Chen and B. Zheng, *Molecules*, 2017, **22**, 57–68.
36 T. M. McIntire and D. A. Brant, *Biopolymers*, 1997, **42**, 133–146.
37 I. S. Yermolenko, V. K. Lishko, T. P. Ugarova and S. N. Magonov, *Biomacromolecules*, 2011, **12**, 370–379.
38 S. Samanta and D. Chaudhuri, *J. Phys. Chem. Lett.*, 2017, **8**, 3427–3432.
39 J. Wang, A. Kulago, W. R. Browne and B. L. Feringa, *J. Am. Chem. Soc.*, 2010, **132**, 4191–4196.
40 C. Kaufmann, D. Bialas, M. Stolte and F. Würthner, *J. Am. Chem. Soc.*, 2018, **140**, 9986–9995.
41 K.-J. Liu and J. L. Parsons, *Macromolecules*, 1969, **2**, 529–533.
42 A. Faraone, S. Magazù, G. Maisano, P. Migliardo, E. Tettamanti and V. Villari, *J. Chem. Phys.*, 1999, **110**, 1801–1806.
43 R. F. Goldstein and L. Stryer, *Biophys. J.*, 1986, **50**, 583–599.
44 P. A. Korevaar, T. F. A. de Greef and E. W. Meijer, *Chem. Mater.*, 2014, **26**, 576–586.
45 J. L. Banal, H. Soleimaninejad, F. M. Jradi, M. Liu, J. M. White, A. W. Blakers, M. W. Cooper, D. J. Jones, K. P. Ghiggino, S. R. Marder, T. A. Smith and W. W. H. Wong, *J. Phys. Chem. C*, 2016, **120**, 12952–12958.
46 S. T. J. Ryan, R. M. Young, J. J. Henkelis, N. Hafezi, N. A. Vermeulen, A. Hennig, E. J. Dale, Y. Wu, M. D. Krzyaniak, A. Fox, W. M. Nau, M. R. Wasielewski, J. F. Stoddart and O. A. Scherman, *J. Am. Chem. Soc.*, 2015, **137**, 15299–15307.
47 G. Wang, W. Wang, R. Miao, C. Shang, M. He, H. Peng, G. He and Y. Fang, *Phys. Chem. Chem. Phys.*, 2016, **18**, 12221–12230.
48 J. Sung, A. Nowak-Król, F. Schlosser, B. Fimmel, W. Kim, D. Kim and F. Würthner, *J. Am. Chem. Soc.*, 2016, **138**, 9029–9032.
49 W. Kim, A. Nowak-Król, Y. Hong, F. Schlosser, F. Würthner and D. Kim, *J. Phys. Chem. Lett.*, 2019, **10**, 1919–1927.
50 E. A. Margulies, J. L. Logsdon, C. E. Miller, L. Ma, E. Simonoff, R. M. Young, G. C. Schatz and M. R. Wasielewski, *J. Am. Chem. Soc.*, 2017, **139**, 663–671.
51 A. L. de Marco, D. Bochicchio, A. Gardin, G. Doni and G. M. Pavan, *ACS Nano*, 2021, **15**, 14229–14241.
52 P. Gasparotto, D. Bochicchio, M. Ceriotti and G. M. Pavan, *J. Phys. Chem. B*, 2020, **124**, 589–599.